Zhang *et al. Energy Mater.* **2025**, *5*, 500116
DOI: 10.20517/energymater.2025.41

Energy Materials

Article

Open Access

Check for updates

Polyol-solid surface/interface transesterification strategy to construct precise anatase/rutile TiO_2 hetero-phase junctions towards enhanced photocatalytic performance

Chengxiang Zhang[1], Yanming Zhou[1], Yang Li[1], Xue Yang[1], Ke Liu[1], Azhar Ayyub[1], Kang Hui Lim[2], Wei Zheng[3], Meisong Xu[1], Wanliang Yang[1,2,*,#], Sibudjing Kawi[2,*,#]

[1]School of Chemistry and Chemical Engineering, Guizhou University, Guiyang 550025, Guizhou, China.
[2]Department of Chemical and Biomolecular Engineering, National University of Singapore, Singapore 119260, Singapore.
[3]Department of Energy and Power Engineering, School of Electrical Engineering, Guizhou University, Guiyang 550025, Guizhou, China.
[#]Authors contributed equally.

[*]**Correspondence to:** Prof. Wanliang Yang, School of Chemistry and Chemical Engineering, Guizhou University, No. 2708 Jiaxiu South Road, Huaxi District, Guiyang, Guiyang 550025, Guizhou, China. E-mail: yangwanlianghhhh@163.com; wlyang@gzu.edu.cn; Prof. Sibudjing Kawi, Department of Chemical and Biomolecular Engineering, National University of Singapore, No. 21 Lower Kent Ridge Road, Singapore 119260, Singapore. E-mail: chekawis@nus.edu.sg

How to cite this article: Zhang, C.; Zhou, Y.; Li, Y.; Yang, X.; Liu, K.; Ayyub, A.; Lim, K. H.; Zheng, W.; Xu, M.; Yang, W.; Kawi, S. Polyol-solid surface/interface transesterification strategy to construct precise anatase/rutile TiO_2 hetero-phase junctions towards enhanced photocatalytic performance. *Energy Mater.* **2025**, *5*, 500116. https://dx.doi.org/10.20517/energymater.2025.41

Received: 20 Feb 2025 **First Decision:** 21 Apr 2025 **Revised:** 12 May 2025 **Accepted:** 26 May 2025 **Published:** 9 Jun 2025

Academic Editor: Ho Won Jang **Copy Editor:** Ping Zhang **Production Editor:** Ping Zhang

Abstract

Heterophase anatase/rutile junctions (A/R-HPJs) in TiO_2 hold significant promise for photocatalysis, yet precise control over phase composition remains elusive. Here, we develop a novel polyol-solid surface/interface transesterification strategy to synthesize TiO_2 A/R-HPJs with tunable mass ratios for photocatalytic seawater splitting and dye degradation. Mechanistic studies reveal that glucose-Ti complexes (GTCs) govern rutile formation, enabling a linear correlation between A/R mass ratios and GTC/Ti molar ratios. Increasing glucose particle surface area via grinding enhances rutile content, evidenced by amplified slope values in this linear relationship. This approach for constructing precise A/R TiO_2 HPJs demonstrates generalizability across diverse polyols, non-solubilizing solvents, and titanium precursors. Phase-dependent carrier separation efficacy is highlighted, with optimized GT15 (optimal A/R ratio) exhibiting exceptional photocatalytic H_2 evolution and pollutant degradation. Our work establishes a surface/interface engineering paradigm for precise heterophase

© The Author(s) 2025. **Open Access** This article is licensed under a Creative Commons Attribution 4.0 International License (https://creativecommons.org/licenses/by/4.0/), which permits unrestricted use, sharing, adaptation, distribution and reproduction in any medium or format, for any purpose, even commercially, as long as you give appropriate credit to the original author(s) and the source, provide a link to the Creative Commons license, and indicate if changes were made.

control in metal oxides, addressing a critical gap in designing functional HPJs for energy and environmental applications.

Keywords: Precise anatase/rutile mass ratio, hetero-phase junction, transesterification strategy, polyol-solid surface/interface, photocatalytic performance

INTRODUCTION

Rampant fossil fuel consumption driven by industrial expansion has triggered dual crises of ecosystem contamination and unsustainable energy dependency[1-3]. These compounding challenges necessitate urgent development of renewable energy systems coupled with advanced pollution mitigation technologies to address interconnected environmental and energy security threats[4,5]. Transitioning to carbon-neutral energy systems now constitutes a critical scientific priority, demanding compatible solutions that integrate environmental friendliness with renewable harvesting efficiency[6,7]. Photocatalytic technology has been recognized as a viable approach for addressing the dual challenges of global energy shortages and environmental degradation through synergistic remediation mechanisms[8,9]. Photocatalysis technology has a wide range of applications, not only for photocatalytic splitting of water into hydrogen but also for pollutant treatment[10]. The photocatalytic efficacy hinges on precise control of nanoscale surface architectures and optimized charge carrier dynamics. These dual determinants dictate redox reaction kinetics through synergistic structural and electronic modulation. The key challenge lies in developing photocatalysts that are both efficient and affordable for the high separation efficiency of photogenerated electron-hole pairs[11,12].

Semiconductor photocatalysis has emerged as a pivotal platform for solar energy harvesting and environmental remediation, driving sustained research efforts over decades[2,8,13]. Transition metal oxides constitute superior photocatalytic platforms due to their tunable photon harvesting efficiency, optimized charge carrier mobility, and tailorable band structures. These inherent advantages enable precise control of redox dynamics through structural engineering. As a prototypical transition metal oxide, TiO_2 offers unique advantages including optimal band alignment, environmental compatibility, and ultraviolet (UV)-spectrum light harvesting[14-17]. Its photocatalytic efficacy is governed by multiple structural parameters spanning phase composition, surface morphology, and crystallographic features[18-20]. Rational architectural control of these interdependent factors enables precise optimization of charge carrier dynamics. Besides, the restriction of recombination between electrons and holes is one of the key issues so as to enhance photocatalytic efficiency of TiO_2. So it is highly desirable to develop approaches that can validly promote charge separation in TiO_2[21,22]. The previous studies almost focus on the architecture-[23], composition-[24,25], facet-[26,27], sensitizing-[28], and composition-control[29,30] of thermodynamically stable crystal phase to improve their photocatalytic performance of TiO_2. Besides, photocatalytic junctions are formed between semiconductors with staggered energy bands. This configuration offers a promising strategy. It boosts photocatalytic efficiency while addressing performance limitations[12,31,32]. The formation of heterojunctions between different materials creates interfaces where charge carriers can be efficiently separated and transferred, reducing recombination, and increasing the quantum efficiency of the photocatalytic process. Several TiO_2-based heterojunctions, including $ZnIn_2S_4/TiO_2$/glass[33], MXene/TiO_2[34], g-C_3N_4/TiO_2[35], MXene/TiO_2/CdS[36], and $ZnIn_2S_4$-Au-TiO_2[37], have been developed for enhancing photocatalytic performance. Notably, homogeneous junctions constructed with the same material[38], such as heterophase junctions and molecular junctions[39], can provide more possible transfer pathways for photogenerated charges. Constructing hetero-phase interfaces offers a doping-free approach to enhance material performance through structural design. This strategy maintains intrinsic material properties while optimizing interfacial charge dynamics. A notable example is the anatase/rutile TiO_2 system (A/R-TiO_2

HPJs). Recent studies demonstrate that interfaces between specific crystalline planes significantly boost charge separation efficiency in photovoltaic devices[40]. The γ/α-MnS heterojunction improves charge transport in batteries[41], while anatase/rutile TiO_2 interfaces promote charge separation in photocatalysis[34]. These architectures simultaneously optimize active sites and electron transfer pathways. Consequently, the strategic design of multiphase interfacial architectures enables precise regulation of charge carrier dynamics, thereby significantly amplifying the redox capacity in photocatalytic systems.

However, the formation of hetero-phase junctions is very challenging, and there is limited research on heterojunctions in the field of photocatalysis. So far, typical methods for synthesizing A/R TiO_2 HPJs include solution-based synthesis[42,43], thermal annealing method[44-46], and physical vapor deposition[47]. Hydrothermal reaction is one of the most widely used solution-based methods to prepare A/R TiO_2 HPJs[46]. Phase composition of A/R TiO_2 HPJs can be regulated by tuning the pH of solution, reactant concentration, reaction temperature and time, additives in a hydrothermal reaction[48,49]. As another effective method to prepare A/R TiO_2 HPJs, solvothermal synthesis is similar to hydrothermal synthesis, but it is conducted in non-aqueous solution. The solvent type in solvothermal synthesis could significantly affect the A/R TiO_2 HPJs[50]. In the thermal annealing method, metal precursors are annealed at high temperatures in air or an inert atmosphere to form A/R TiO_2 HPJs. The annealing temperature has been revealed to be significant in controlling the phase of the products. Physical vapor deposition is a widely used technique to deposit thin films on substrates. In this process, the materials to be deposited first transform into the vapor state through a physical process and then transform back to the solid state by forming a thin film. Although the high-temperature hetero-phase junctions synthesis of A/R TiO_2 HPJs dates back to the 1970s[51], almost all methods of inducing phase transitions partially by calcination have had difficulty in precisely controlling the mass ratio of the crystal phase. The main approach to this problem is to introduce an acidic environment and a ligand (e.g., HCl, HOAc, *etc.*) into the solution reaction to mediate the coordination mode of Ti^{4+} and thus control the final crystalline phase. While solution-based reactions can compensate for this shortcoming, the harsh muti-step reactions in the synthesis process are very dependent on the experience of the researchers, limiting the expansion of their potential applications. Commercial P25, the benchmark photocatalyst, is synthesized via vapor-flame aerosol deposition. This method necessitates specialized equipment and intricate process control, limiting its scalability for industrial applications. Moreover, it is hard or impossible to control the phase ratio[52]. Therefore, there is an urgent need for a simple and universal synthesis route to produce A/R TiO_2 HPJs with highly controllable crystal phase selectivity at a low cost and sustainably.

To address these challenges, we developed a novel and straightforward polyol-solid interface transesterification strategy that enables precise control over the anatase-to-rutile (A/R) phase ratio in TiO_2 nanostructures. Central to this approach is the formation of glucose-Ti complexes (GTCs) through surface-mediated transesterification, which serve as critical modulators for rutile phase stabilization. By employing glucose as a hydroxyl-rich polyol template and systematically modulating the transesterification reaction kinetics, we synthesized intermediate TiO_2 phases (denoted as Gx) with varying GTC concentrations. Through optimization of the G/Ti molar ratio [glucose to titanium butoxide (TBOT)], this strategy achieves unparalleled phase composition control, permitting continuous tuning of crystal phase fractions from pure anatase (0% rutile) to pure rutile (100% rutile) configurations. Our mechanistic analysis suggests that the available surface area of glucose particles acts as a governing parameter for the A/R phase mass ratio, establishing a direct structure-directing relationship between the polyol template morphology and final crystalline architecture. Experimental results indicate that, after glucose grinding, the slope of the linear relationship between the R/A phase mass ratio and the G/Ti increases, which confirms that the increase in the surface area of glucose solids can enhance the content of rutile. In addition, polyol-solid surface/

interface transesterification strategy to construct precise anatase/rutile TiO_2 hetero-phase junctions can be universally applied to other polyols solid [fructose, sucrose, D-(+)-trehalose], solvent that cannot dissolve solid polyols (Petroleum ether, n-octane, methanol), and titanium sources [Tetraisopropyl titanate (TTIP), TBOT]. As expected, proof-of-concept application for crystal phase-dependent of A/R TiO_2 HPJs shows that the obtained GT15 (it represents a molar ratio of glucose to TBOT of 15:1) exhibits enhanced performance in photocatalytic HER from seawater splitting; the highest H_2 production rates reached 5,787.7 $\mu mol \cdot h^{-1} \cdot g^{-1}$, which was 4.37 and 253.85 times higher than that of pure anatase and pure rutile, respectively. Meanwhile, without any co-catalyst, GT15 also demonstrated the best photocatalytic performance, degrading 98.17% of Rhodamine B (RhB) at a concentration (20 mg/L) within 90 min. Enhanced photocatalytic performance of GT15 is attributed to the maximization of anatase/rutile interfacial contact, which facilitates efficient separation and transfer of photogenerated carriers. Collectively, this work establishes a fundamental framework for crystal phase engineering in oxide materials, offering mechanistic insights and programmable design principles that advance precise compositional control in heterogeneous catalysis systems. The demonstrated strategy opens new avenues for tailoring phase-dependent material functionalities through surface-mediated reaction dynamics.

EXPERIMENTAL

Chemicals

All of the chemical reagents used in this paper are listed in Supplementary Table 1.

Preparation of A/R TiO_2 HPJs photocatalysts

A strategy of polyol-solid surface/interface transesterification was used to synthesize A/R TiO_2 HPJs GTx (x = 0, 5, 10, 20, 30 and 35). Usually, in a waterless environment, take 4 mL TBOT at room temperature and mix it evenly in 50 mL n-octane to form a transparent solution. Subsequently, glucose was added to the system and stirred for 10 min, and then transferred to a rotary evaporator for distillation under reduced pressure at 80 °C for 1 h to obtain GTC adsorbed by excess TBOT. The intermediate Gx (x = 0, 5, 15, 20, 30 and 35) was obtained by exposing the product to air at room temperature for another 30 min. Finally, the A/R TiO_2 HPJs GTx was obtained by annealing the intermediate Gx at 450 °C for 3 h at a heating rate of 5 °C/min in a muffle furnace. By fixing the amount of TBOT and adjusting the amount of glucose at the same time, the molar ratio of glucose to TBOT can be adjusted, and finally different TiO_2 hetero-phase junctions with different anatase to rutile ratios can be obtained.

The specific experimental procedures of characterizations, photocatalytic H_2 evolution tests and Photocatalytic dye degradation tests were listed in the Supporting Information.

RESULTS AND DISCUSSION

The synthesis of anatase/rutile TiO_2 heterophase junctions (denoted as GTx) was accomplished via a two-step protocol illustrated in Figure 1A. A fixed volume of TBOT (4 mL) was dispersed in n-octane while varying glucose quantities established the G/Ti ratio. Given glucose's insolubility in n-octane, it remained solid-phase throughout the reaction. During rotary evaporation at 80 °C, surface/interface transesterification occurred between TBOT and hydroxyl groups (-OH) on glucose particles, generating GTCs. This reversible reaction was driven to completion through continuous removal of the n-butanol by-product via negative pressure evaporation, facilitated by its low boiling point.

Unreacted TBOT molecules persisted on GTC surfaces due to their high volatility threshold (> 310 °C), remaining non-volatile during rotary evaporation and ambient storage. These residual TBOT molecules subsequently underwent spontaneous hydrolysis in air, forming amorphous TiO_2 coatings. The GTC core

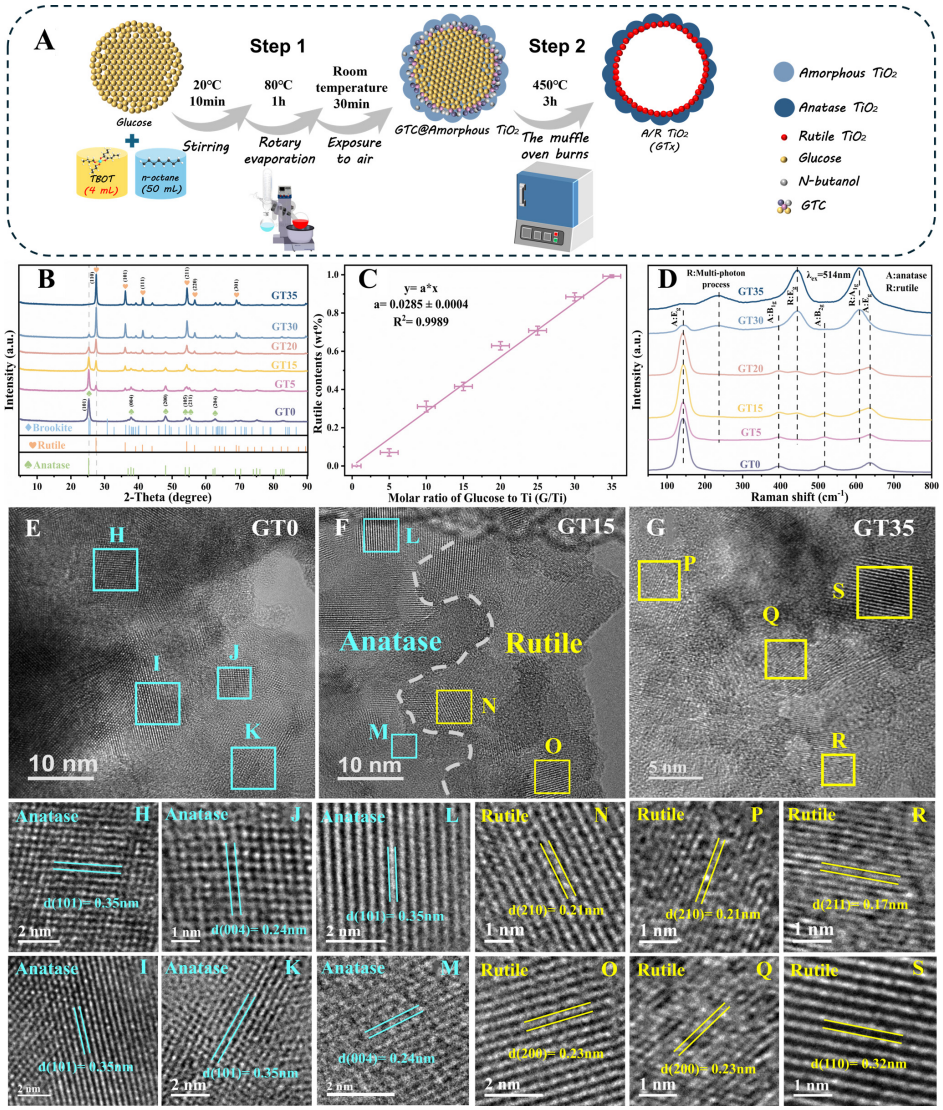

Figure 1. (A) Schematic of the synthetic procedure for the synthesis of GTx HPJs from intermediates Gx (x is the molar ratio of glucose to TBOT, x = 0, 5, 15, 20, 30, 35); (B) XRD patterns of GTx HPJs; (C) The linear relationship between the mass fraction of rutile phase and G/Ti in GTx HPJ with glucose microcrystal as raw material; (D) Raman spectra with excitation line at 514 nm for GTx HPJs; (E) HRTEM images of GT0, (F) GT15 and (G) GT35; (H-S) show the close observations to the areas highlighted by yellow and cyan boxes in Figure 1E-G. TBOT: Titanium butoxide; XRD: X-ray diffraction; HRTEM: high-resolution transmission electron microscopy; GTx HPJs: anatase/rutile TiO_2 hetero-phase junctions.

demonstrated remarkable atmospheric stability against hydrolysis. Subsequent annealing at 450 °C induced phase differentiation: GTCs transformed into rutile-phase TiO_2 while surface-adsorbed amorphous TiO_2 crystallized into anatase-phase TiO_2. This thermally driven phase segregation yielded well-defined anatase/rutile heterojunctions with coherent interfaces.

X-ray Diffraction (XRD) analysis verified the crystallographic phase purity of synthesized photocatalysts, with characteristic diffraction patterns confirming both chemical composition and lattice structure. Figure 1B shows the XRD patterns of a series of TiO_2 photocatalysts with different phase compositions. The XRD analysis of GT0 revealed prominent diffraction features at 25.3°, 37.8°, 48.0°, 53.8°, 55.0°, and 62.6°, systematically indexed to the (101), (004), (200), (105), (211), and (204) crystallographic orientations of

anatase TiO_2 (JCPDS card No. 21-1272), respectively[53]. This proves that the crystal phase of GT0 is composed of pure anatase phase. XRD analysis of G5-G30 demonstrated progressive emergence of diffraction features at 27.4°, 35.9°, 41.1°, 54.1°, 56.6°, and 69.0°, corresponding to the (110), (101), (111), (211), (220), and (301) crystallographic reflections of rutile TiO_2 (JCPDS 21-1276)[54]. This phase evolution correlated directly with incremental glucose loading. When the G/Ti reaches 15:1, the mass ratio of anatase to rutile in sample GT15 reaches 68.46:31.54. This result suggests that GT5, GT15, GT20 and GT30 have miscible structures where anatase and rutile phases coexist. When G/Ti reaches 35:1, the diffraction peaks belonging to anatase phase in sample GT35 disappear, which marks the successful synthesis of pure rutile TiO_2. From 0:1 to 35:1, as the G/Ti increases, the diffraction intensity of the rutile phase gradually increases while that of the anatase phase gradually decreases, indicating that the content of rutile in A/R TiO_2 is highly tunable during the process of increasing G/Ti. The mass fraction of rutile to anatase TiO_2 phases was determined by[55]

$$W_R = A_{rutile}/(0.886*A_{anatase} + A_{rutile}) \quad (1)$$

where W_R represents the weight percentage of rutile TiO_2, and $A_{anatase}$ and A_{rutile} denote the integrated peak areas corresponding to the anatase (101) and rutile (110) XRD reflections, respectively [Supplementary Table 2].

Based on the analyses conducted using XRD and the analysis results of experimental data, it is found that there is a correlation between the content of rutile in A/R TiO_2 and the G/Ti. From the synthesis process, it can be seen that the more GTC, the more rutile phase content in A/R TiO_2 HPJs. Our study reveals that the rutile phase content in the A/R TiO_2 HPJs ranges from 0 wt/% to 100 wt% as the molar ratio between glucose and TBOT varies from 0 to 35. Analysis of the experimental data indicates a linear relationship, with a fitted line exhibiting a slope of 0.0285 ± 0.0004 and an R-squared value of 0.9989, demonstrating a strong positive correlation between the G/Ti and the rutile content [Figure 1C]. Due to the insolubility of glucose in the non-polar solvent C_8H_{18}, it is obvious that this pronounced positive correlation can be attributable to the surface/interface control of the glucose particles. As the amount of glucose increases, the number of surfaces/interfaces available for transesterification reactions also rises incrementally. The linear correlation coefficient R-squared value, which is closely approaching 1, confirms this viewpoint. Thus, by specifying the desired rutile phase content in A/R TiO_2 HPJs, researchers can determine the corresponding G/Ti, thereby allowing for precise control over the mass ratio of phase composition.

Raman spectroscopy enables precise discrimination of anatase and rutile TiO_2 polymorphs. Visible laser-excited spectral analysis delivers critical insights into surface phase composition, enabling direct correlation with GTx's crystallographic characteristics. Visible Raman spectroscopy of GT5-GT30 samples [Figure 1D], exhibited characteristic anatase TiO_2 bands at 143, 395, 515, and 633 cm^{-1}, assigned to the E_g, B_{1g}, B_{2g} and E_g Raman-active modes, respectively[55,56]. Additional features at 243, 445, and 613 cm^{-1} were attributed to multi-phonon scattering processes and the E_g and A_{1g} vibrational modes of rutile TiO_2. These results demonstrated the anatase-rutile structure coexists in GT5, GT15, GT20, and GT30. For the samples GT0 and GT35, the Raman characteristic peaks belonging to rutile and anatase respectively disappeared completely, which indicates that these samples comprise a single phase. These findings confirmed the progressive enhancement of rutile phase content in GTx with elevated G/Ti ratios, demonstrating the successful fabrication of A/R TiO_2 HPJs featuring precisely tunable crystalline phase configurations, consistent with XRD analyses.

High-resolution transmission electron microscopy (HRTEM) images in Figure 1E-G reveal the microstructure of three typical samples, G0, G15, and G35. All three samples have clear lattice stripes, indicating that they are highly crystalline, with no evidence of additional phases or amorphous material. Enlarged views of different areas in Figure 1E-G are shown in Figure 1H-S. Clear lattice fringes at 0.35 nm and 0.24 nm, corresponding to (101) plane and (004) plane of anatase, could be observed in Figure 1H-K, revealing the crystal structure and interfacial atom arrangement of GT0. Conversely, the analysis of sample GT35 shows that the measured facet spacings of 0.21, 0.23, 0.17, and 0.32 nm correspond closely to the d(210), d(200), d(211), and d(110) planes of rutile, respectively [Figure 1P-S][34,48]. The above data show that GT0 is a typical pure anatase TiO_2 structure, while GT35 has the characteristics of pure rutile TiO_2, consistent with XRD data and Raman data [Figure 1B and C]. The HRTEM image of sample GT15 reveals that the (101) and (004) planes of anatase, as well as the (210) and (200) facets of rutile, exhibit high crystallinity and are well-interconnected, demonstrating a good lattice match, which is indicated that GT15 has anatase/rutile TiO_2 heterojunction structure. In addition, selected area electron diffraction (SAED) analysis conducted on GT15 revealed two distinct diffraction ring series, corresponding to anatase and rutile phases, respectively [Supplementary Figure 1][48]. The results presented above provide direct evidence for the successful formation of A/R TiO_2 HPJ, which aligns with the observations obtained from XRD and Raman spectroscopy.

Based on the experimental results [Figure 1], we propose a novel polyol-solid surface/interface transesterification strategy to elucidate the precise control of TiO_2 crystal phase composition. Notably, GTCs serve as the critical determinant for rutile formation, making the complete conversion of TBOT into GTCs essential. Given that the transesterification between glucose and TBOT is reversible, the removal of by-product n-butanol through Le Chatelier's principle enables more thorough reaction progression. During heating and rotary evaporation, TBOT molecules adsorbed on the surface of glucose solid particles continue to react with abundant surface -OH groups, ultimately converting into GTCs on the glucose particle surfaces. It should be emphasized that the surface-bound GTCs exhibit hydrolysis resistance in air, while residual TBOT adsorbed on the glucose surfaces readily hydrolyzes to form amorphous TiO_2. Subsequent high-temperature (450 °C) calcination converts GTCs into rutile phase and transforms the surrounding amorphous TiO_2 into anatase phase, ultimately establishing a rutile/anatase heterojunction structure. According to this principle, when no glucose is added [Figure 2A1], the TBOT after solvent evaporation is completely hydrolyzed in the air, forming amorphous TiO_2 [Figure 2A2], and after annealing, anatase TiO_2 is obtained [Figure 2A3]. As the G/Ti increases, TBOT undergoes transesterification on the surface/interface of the glucose particles [Figure 2B1], and after the solvent has completely evaporated, the surface of the glucose has reacted with TBOT, forming glucose particles completely encapsulated by GTC. Excess TBOT molecule is adsorbed on the surface of GTC; after hydrolysis in the air, amorphous TiO_2-coated GTC particles Gx are obtained [Figure 2B2]. After annealing to remove glucose, anatase-TiO_2-coated rutile TiO_2 cavities are obtained [Figure 2B3]. When the G/Ti increases to 15:1, all excess TBOT is completely adsorbed on the surface of the GTC [Figure 2C1]. Through the hydrolysis process in the air, amorphous TiO_2 is formed, which perfectly encapsulates the GTC-glucose particles [Figure 2C2]. The final product is straticulate anatase encapsulated A/R TiO_2 HPJs GT15 synthesized through the annealing process in the air [Figure 2C3]. As the G/Ti continues to increase, the excess TBOT accounts for a smaller proportion compared to GTC [Figure 2D1]. This portion of TBOT is adsorbed onto the surface of GTC during the rotary evaporation process, and after a placing process in the air, amorphous TiO_2 is dotted on the outer surface of GTC [Figure 2D2], resulting in a smaller amount of anatase TiO_2 dispersed on a larger surface of rutile TiO_2 in the GT30 sample after annealing [Figure 2D3]. When the G/Ti further increases to 35:1, all TBOT achieves uniform dispersion on the surface of glucose particles and is completely converted to GTC [Figure 2E1]. However, GTC cannot be hydrolyzed into amorphous TiO_2 in the air [Figure 2E2]. After the annealing process, it is entirely transformed into rutile TiO_2 [Figure 2E3]. Therefore, this work has achieved

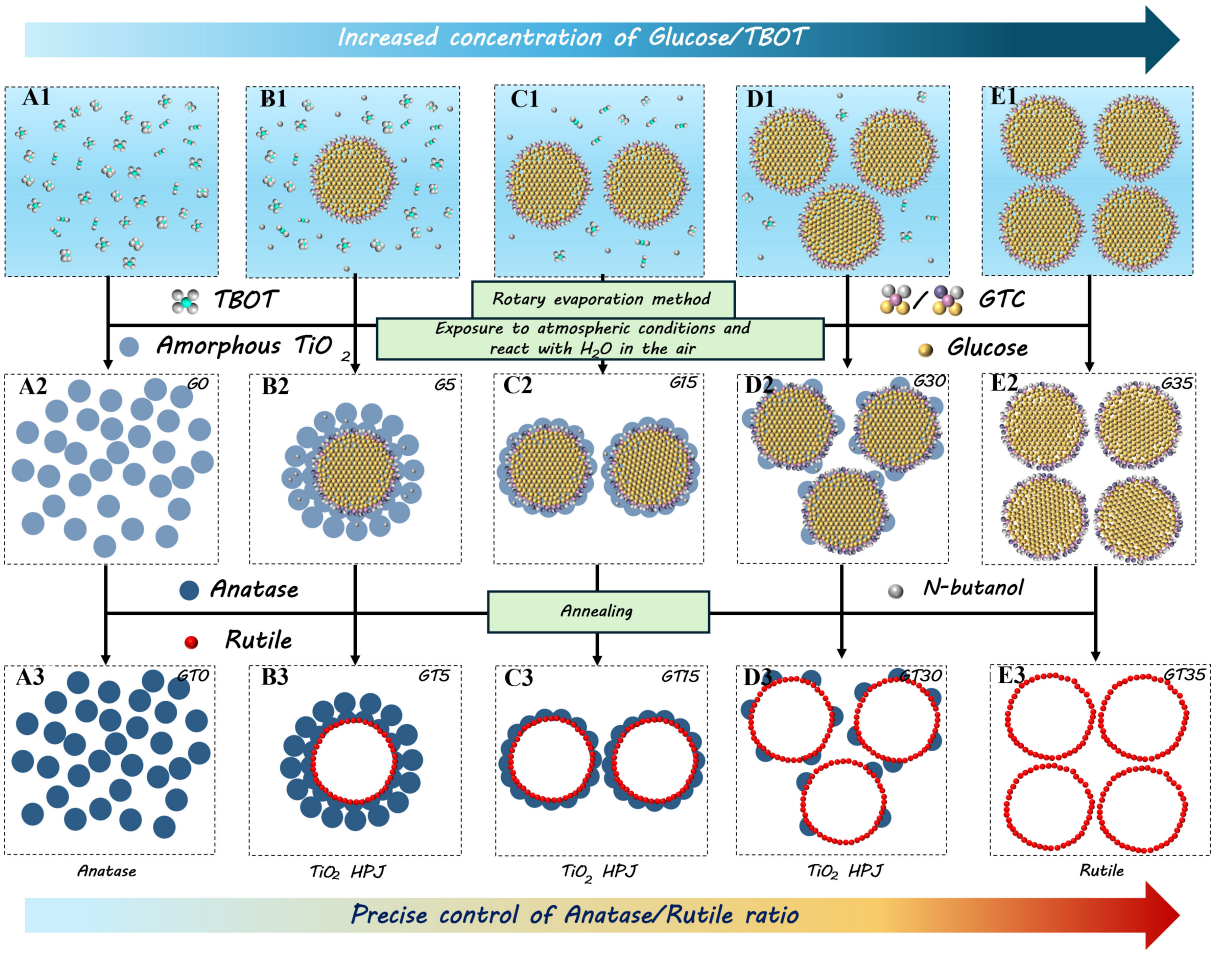

Figure 2. Schematic representation of the polyol-solid surface/interface transesterification strategy used to construct intermediate Gx in different states to regulate the phase composition. Synthesis methods: (A1) uncomplexed TBOT, (B1-D1) the transesterification reaction between TBOT and glucose surface/interface resulted in the formation of GTC with different amounts of TBOT adsorbed on the surface; (E1) Intermediate pure GTC of GT35, which is completely transesterification reactive on the glucose surface/interface and contains no TBOT; (A2) Amorphous TiO_2 G0 formed after hydrolysis of TBOT in air; (B2-E2) Intermediates G5, G15, G30, and G35; (A3) Anatase TiO_2 formed from amorphous TiO_2 by annealing in air; (B3-D3) A/R TiO_2 HPJs with different phase mass ratios formed by annealing in air to remove glucose. (E3) Rutile TiO_2 formed by annealing in air. TBOT: Titanium butoxide; GTC: glucose-Ti complexes.

precise and controllable regulation from anatase TiO_2 to rutile TiO_2.

To further enhance the understanding of this crystal phase mass ratio regulation process mediated by polyol-solid surface/interface transesterification, scanning electron microscopy (SEM) was employed to observe the morphology of the typical intermediates G15, G30 and G35, respectively. As revealed in Figure 3A-D, the micromorphology of the samples remained hardly unchanged following the transesterification, relative to the glucose. The SEM images of G15, G30, and G35 [Figure 3B-D] indicate that, compared to GT30 or GT35, GT15 exhibited the highest degree of particle adhesion, which could be attributed to the highest amorphous TiO_2 content among the three.

Given that Gx is insoluble in most deuterium reagents, the chemical environment was analyzed using ^{13}C solid-state nuclear magnetic resonance (^{13}C SSNMR). Based on the ^{13}C SSNMR signal assignments [Figure 3E], it is evident that most carbon atoms (carbon nuclei 1-6) in glucose exhibit chemical shifts between 50 and 120 ppm, with the presence of several distinct peaks. The newly observed signals in the

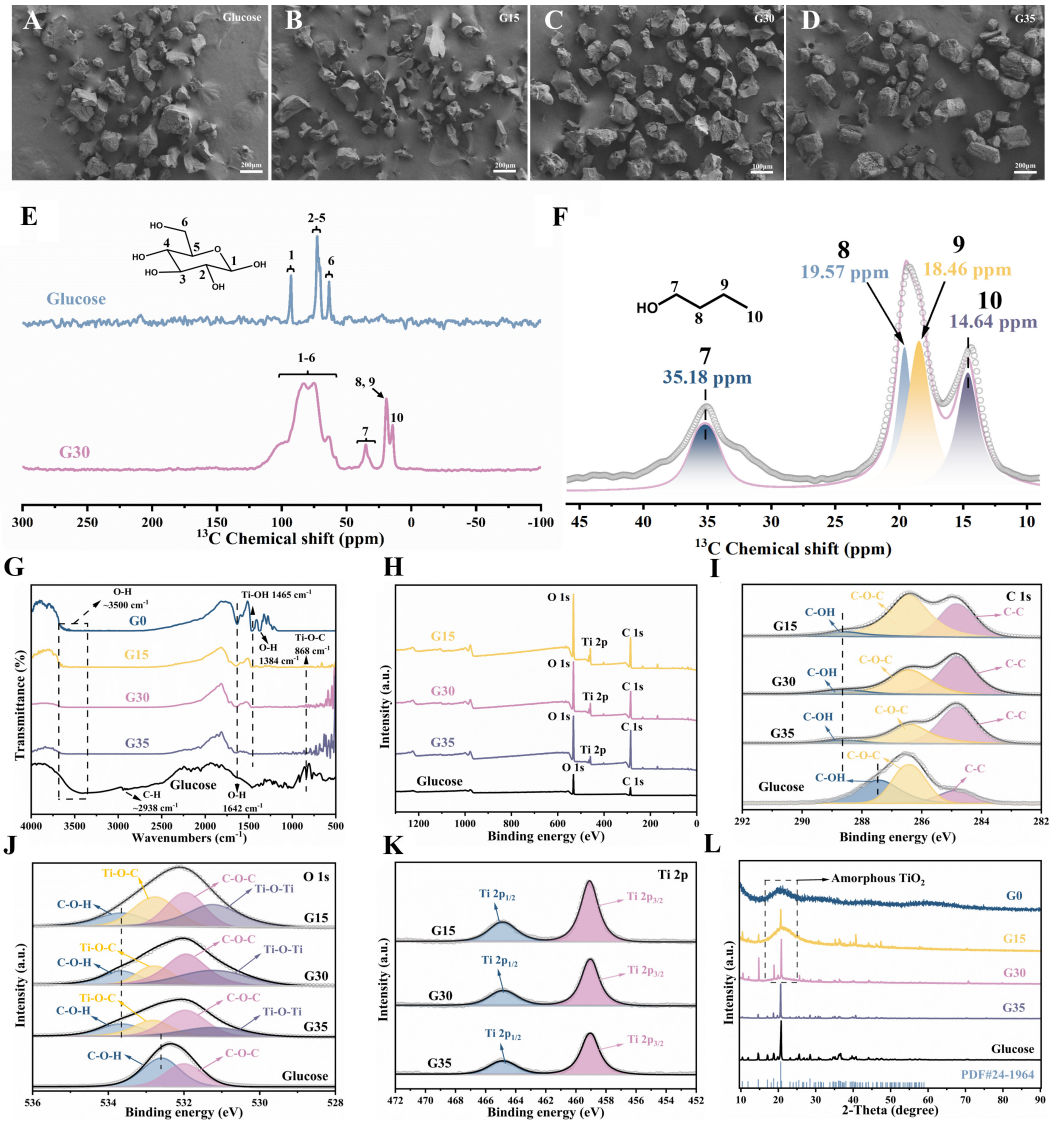

Figure 3. SEM images of (A) glucose, (B) intermediates G15, (C) intermediates G30 and (D) intermediates G35; (E) ^{13}C SSNMR spectrum, and signal assignment of glucose and the intermediate G30; (F) Magnified ^{13}C SSNMR signal of by-product $C_4H_{10}O$ in Figure 3E; (G) FT-IR spectra of glucose and Gx (x=0, 15, 30, 35); XPS spectra of (H) survey, (I) C 1s, (J) O 1s, and (K) Ti 2p for G15, G30, G35 and glucose; (L) XRD patterns of glucose, G0, G15, G30 and G35. SEM: Scanning electron microscopy; XRD: X-ray diffraction; ^{13}C SSNMR: ^{13}C solid-state nuclear magnetic resonance; FT-IR: fourier transform infrared spectroscopy; XPS: X-ray photoelectron spectroscopy.

range of 10 ppm to 50 ppm were ascribed to the by-product $C_4H_{10}O$ encapsulated within amorphous TiO_2[57]. As shown in Figure 3F, the signal with a chemical shift of 35.08 ppm is attributed to carbon nuclei 7. The signals from the carbon nuclei were observed to split into two distinct components: one at 19.47 ppm, while the other displayed a new peak at 18.35 ppm, corresponding to carbon nuclei 8 and 9, respectively[58,59]. The chemical shift of carbon nuclei 10 is observed at approximately 14.64 ppm. Following the surface/interface transesterification, the initially discrete signals with chemical shifts in the range of 50-100 ppm were merged into a combined signal. This combination is attributed to the fact that the carbon nuclei in the resulting GTC exhibit similar chemical shift values. Subsequent to the transesterification, the originally distinct signals with chemical shifts ranging from 50 ppm to 100 ppm were converted into a combined signal. This merging is ascribed to the similarity in chemical shift values of the carbon nuclei in

the resulting GTC, thereby indicating the successful synthesis of GTC following the transesterification.

Fourier transform infrared spectroscopy (FT-IR) was employed to characterize the surface functional groups of intermediate species, as presented in Figure 3G. The peaks observed at 2,938 cm^{-1} are attributed to the stretching vibration of the C-H alkyl groups in glucose[60]. For samples G0, G15, and G30, the peak observed at 1,465 cm^{-1} is assigned to the Ti-OH bond on the surface of amorphous TiO_2. In contrast, the relatively weak Ti-OH peak in sample G35 is attributed to the presence of surface hydroxyl group of GTC. From G0 to G35, the Ti-OH vibration peak at 1,465 cm^{-1} gradually decreases, indicating that the Ti-OH characteristics of amorphous TiO_2 on the surface of GTC gradually disappear with the deepening of transesterification. The broad peak located at about 3,500 cm^{-1} is assigned to the O-H of glucose[61,62]. Compared to G0, samples G15, G30 and G35 showed a characteristic peak of Ti-O-C stretching vibration appears at 868 cm^{-1} after the surface/interface transesterification reaction, indicating the successful synthesis of GTC.

To gain deeper insight into the surface chemical states of the intermediates G15, G30 and G35, the prepared samples were subjected to X-ray photoelectron spectroscopy (XPS) analysis. As illustrated in Figure 3H, the elemental signals for C, O, and Ti are present in all samples, with no evidence of additional impurities. The C 1s peaks of all intermediates were deconvoluted into three species centered at 288.6, 286.4, and 284.8 eV, belonging to C-OH, C-O-C, and C-C, respectively [Figure 3I][54,63]. As the transesterification progressed, the abundant C-OH groups on the surface/interface of solid glucose were progressively transformed into Ti-O-C, resulting in a gradual diminution of the C-OH peak intensity. The O 1s peak of glucose in Figure 3J was deconvoluted into two characteristic peaks centered at 532.7 and 532.1 eV, corresponding to C-O-H and C-O-C, respectively, and after the formation of the GTC, the peaks appeared at 533.6, 532.8, 532.0, and 531.2 eV, corresponding to C-O-H, Ti-O-C, C-O-C, and Ti-O-Ti, respectively[64-66]. In contrast to the glucose particles, Ti-O-Ti bonds were observed in all intermediates. This presence can be ascribed to the formation of amorphous TiO_2 in samples Gx (where x = 15, 30) and to the connection mode of GTC in sample G35. From GT15 to GT35, the newly appeared Ti-O-C peak at 532.8 eV indicates the successful transesterification reaction, which is consistent with the findings of ^{13}C SSNMR and FT-IR. The inverse proportionality between binding energy shifts and electron cloud density rationalizes the detected displacements of C-O-H signatures in O 1s (533.6 eV) and C 1s (288.6 eV) spectra for Gx samples (x = 15, 30, 35) compared to pristine glucose (532.7, 287.6 eV). These spectroscopic shifts originate from interfacial coordination bond formation between TBOT and glucose surfaces through Ti-O-C linkages. The Ti 2p core level spectrum was resolved into spin-orbit split components (Ti $2p_{3/2}$ and Ti $2p_{1/2}$) with a constrained 2:1 area ratio and 5.7 eV spin-orbit splitting, as shown in Figure 3K. The binding energy levels of 464.9 eV for Ti $2p_{3/2}$ and 459.2 eV for Ti $2p_{1/2}$ are indicative of the Ti^{4+} oxidation state[67,68], implying that the transesterification process does not induce a change in the Ti valence state.

To verify the composition of the intermediates more conclusively, XRD analyses were conducted on a series of intermediates designated as Gx (x = 0, 15, 30 and 35). The XRD patterns of the series of intermediates [Figure 3L] reveal progressively distinct diffraction peaks. Sample G0 exhibits a broad peak between 18° and 25°, indicative of amorphous TiO_2. In contrast, samples G15, G30, and G35 display sharp diffraction peaks at 18.9°, 19.9°, and 20.7°, corresponding to the (011), (101), and (111) crystal planes of glucose (JCPDS card No. 24-1964), respectively. The intensity of the glucose characteristic peaks in the intermediates increases with the G/Ti, while the amorphous TiO_2 content decreases until its disappearance. In sample G35, amorphous TiO_2 is completely absent, suggesting that all TBOT have fully participated in transesterification with the -OH on glucose surface/interface, forming GTC. The above results provide direct evidence for the mechanism described in Figure 2.

To delve deeper into the annealing process of intermediate substances in air, three characteristic intermediates, designated as G15, G30 and G35, were chosen for analysis using thermogravimetric-infrared (TG-IR) spectroscopy. Figure 4A-C presents the infrared spectra of the volatile compounds emanating from the pyrolysis reactions of these selected intermediates. Absorption bands indicative of O-H stretching and in-plane bending vibrations were observed in the range of 3,500-4,000 cm^{-1} and 1,250-1,500 cm^{-1}, respectively, across the temperature spectrum of 117.5-600 °C [Figure 4D-F][69,70].

These bands are associated with the volatilization of either free water or crystallization water. Moreover, absorption bands characteristic of C=O stretching vibrations in aldehydes were noted between 1,030-1,110 cm^{-1} and 1,600-1,850 cm^{-1} at temperatures ranging from 100-350 °C. Additionally, absorption bands corresponding to C=O stretching and out-of-plane bending vibrations of carbon dioxide were identified near 2,280-2,400 cm^{-1} and 670 cm^{-1}, respectively, within a temperature range of 100-600 °C[71]. These observations can be attributed to the carbonation and decomposition of the organic compound glucose. Interestingly, compared to G30 and G35, G15 reaches the peak CO_2 release significantly later than G30 and G35 in the temperature range of 500 °C to 550 °C, which can be attributed to the fact that the anatase TiO_2 layer converted by amorphous TiO_2 hinders the CO_2 release. Moreover, characteristic saturated and unsaturated C-H stretching vibrations were detected in the range of 2,770-3,050 cm^{-1} at temperatures between 117.5 and 350 °C[72]. These vibrations are attributable to the volatilization and decomposition of residual $C_4H_{10}O$ as a by-product in amorphous TiO_2. From G15, G30 to G35, the vibration peaks at 2,770-3,050 cm^{-1} gradually disappear, indicating a significant decrease in the volatilization of $C_4H_{10}O$, which is attributed to the increase in the number of the surface of glucose particles promoting a more complete transesterification. These results are consistent with the mechanism described in Figure 2.

Figure 4G-I illustrates the annealing of Gx precursors to synthesize TiO_2 HPJs and documents the thermogravimetric (TG) and differential thermal analysis (DTA) curves associated with the pyrolysis process. Notably, the highest pyrolysis residue was observed in the G0 sample, the lowest in the G35 sample, and no residue in glucose following identical pyrolysis conditions. This suggests that the surface of glucose in the G15 intermediate was most effectively utilized, retaining a substantial amount of amorphous TiO_2 compared to the other two intermediates. When the G/Ti ratio was 15:1 (G15), the intermediate contained the lowest proportion of GTC and the highest amorphous TiO_2 content due to the fixed TBOT volume (4 mL). The abundant amorphous TiO_2 encapsulation hindered complete CO_2 release during pyrolysis, resulting in higher residual mass for G15. As the G/Ti ratio increased (G30, G35), the GTC proportion in intermediates rose, while amorphous TiO_2 vanished gradually. This shift enabled more thorough thermal decomposition in G35, yielding the lowest residual mass.

The differential thermogravimetric (DTG) curves exhibited four distinctive peaks at ambient temperature, specifically at approximately 170 °C, between 170-210 °C, 210-350 °C, and 350-600 °C [Figure 4G]. The pyrolysis process was categorized into four sequential stages (Stages I-IV) based on the patterns observed in the DTG curves. In Stage I (from ambient temperature to 150 °C), the weight loss primarily arises from the volatilization of $C_4H_{10}O$ and the expulsion of water of crystallization. Stage II (150-210 °C) is primarily governed by the decomposition of the by-product $C_4H_{10}O$, findings that align with the FT-IR data on gases emitted during pyrolysis [Figure 4A-F]. Stage III (210-350 °C) is marked by the maximum weight loss across all samples, which is attributable to the pyrolysis of glucose in an oxidative atmosphere. The complete breakdown of glucose, transforming entirely into CO_2, occurs in Stage IV (350-600 °C). This final stage also sees the progressive crystallization of TiO_2, leading to the formation of the ultimate TiO_2 HPJs. The above results further fully demonstrate that the ratio of amorphous TiO_2 and GTC in the intermediate can be achieved by simply adjusting the G/Ti ratio through the transesterification between TBOT and the surface

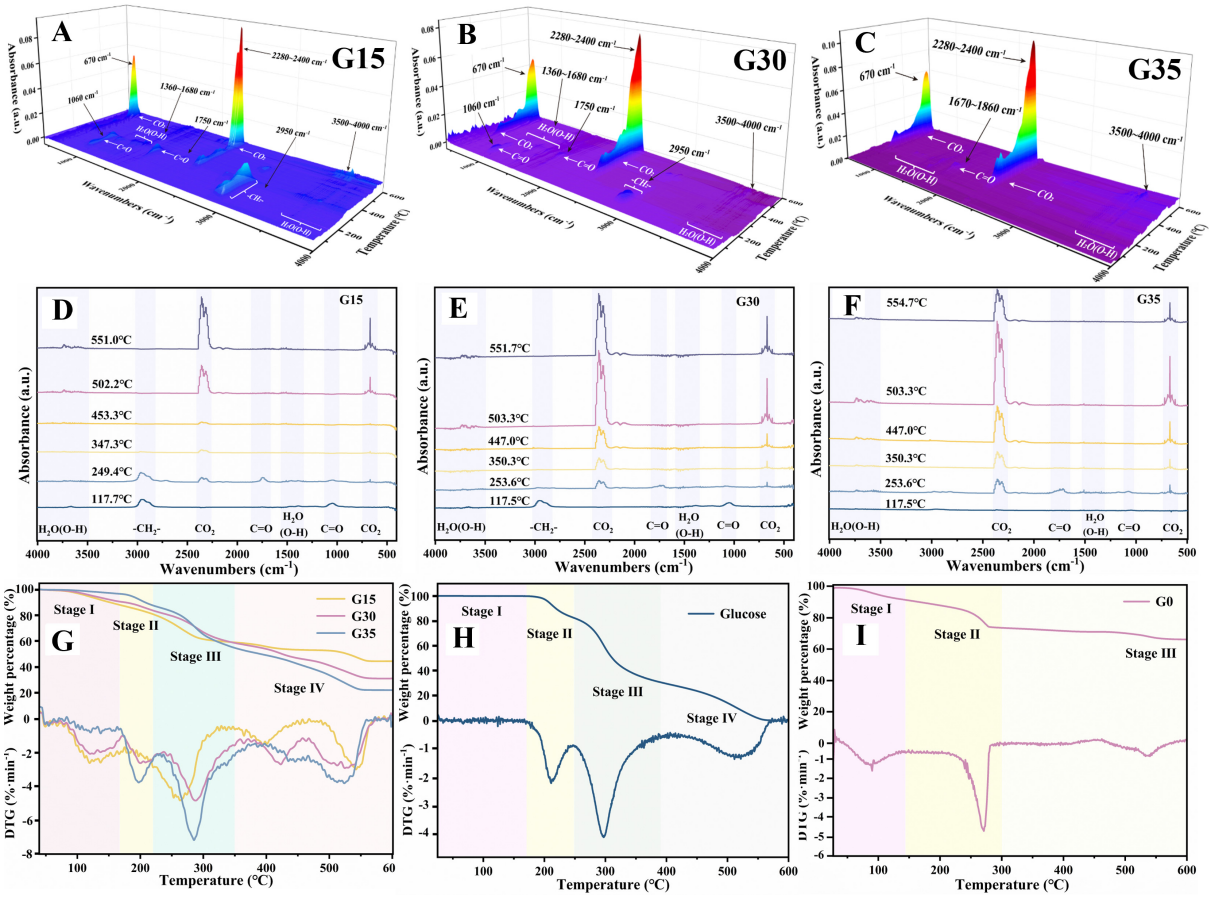

Figure 4. FT-IR spectrum of the volatile matter from (A and D) intermediates G15, (B and E) G30, and (C and F) G35 under air atmosphere; (G and H) TG/DTG curves of intermediates G15, G30, G35 and glucose; (I) TG/DTG curves of intermediate G0. FT-IR: Fourier transform infrared spectroscopy; TG/DTG: thermogravimetric/differential thermogravimetric.

of glucose particles.

To assess the surface area correlation of polyol-solid surface/interface transesterification strategy, a series of A/R TiO_2 with different phase compositions were synthesized using glucose microcrystals that had been ground to substantially reduce grain size [Figure 5A]. Particle size distributions before and after grinding are shown in Supplementary Figure 2, and the average particle size is significantly reduced during grinding. As shown in Figure 5B, the A/R TiO_2 HPJs obtained after grinding (marked as AG-GTx, x= 0, 3, 15, 25, 30 and 35) still show a similar trend of crystal phase ratio change as before grinding [Figure 1B]. It is worth noting that since AG-GT30, it has shown the characteristics of pure rutile TiO_2, and the G/Ti required to achieve pure rutile TiO_2 is obviously less than that of ungrounded glucose. This result can be attributed to the fact that the grinding process exposes more of the outer surface area of the glucose particles. This is also shown by the increase in the slope of the fitted straight line [Figure 5C].

In order to further evaluate the universality of polyol-solid surface/interface transesterification strategy, in this study, the substrate range was explored in an expansive manner. Firstly, the effect of solvents of different polarities on the transesterification reaction was explored [Figure 5D]. A G/Ti of 30:1 was chosen as the baseline for all substrate expansion experiments. When the solvent of the reaction system was ethanol, although the annealed product GT30-EtOH also showed a tendency towards an increase in the

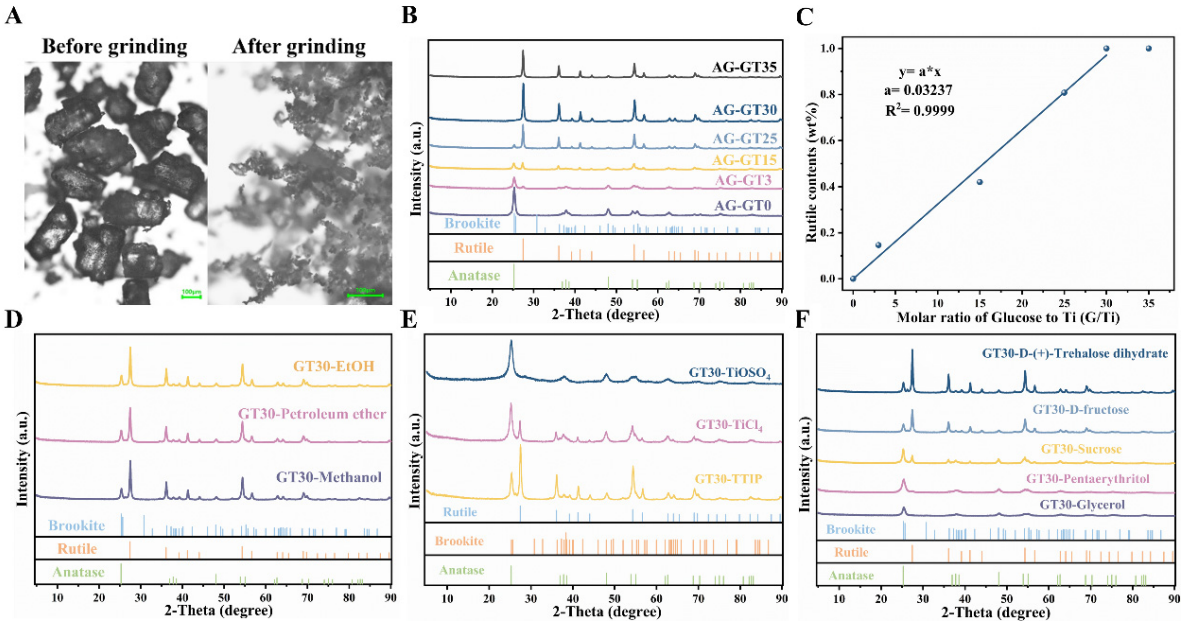

Figure 5. (A) Polarizing microscope images of glucose crystals before/after grinding; (B) XRD patterns of AG-GTx HPJs (x = 0, 3, 15, 25, 30, 35) obtained from glucose microcrystals after grinding operation; (C) The linear relationship between the mass fraction of rutile phase and G/Ti in AG-GTx with glucose microcrystals obtained after grinding operation; (D) XRD images of GT30 synthesized with solvents of different polarity; XRD patterns of GT30 synthesized by different substrates: (E) Ti sources (F) Various Polyols. XRD: X-ray diffraction; AG-GTx HPJs: anatase/rutile TiO_2 hetero-phase junctions synthesized with after-grinding glucose.

rutile phase, the pure phase of rutile TiO_2 could not be obtained when the G/Ti was further increased to 35:1 [Supplementary Figure 3]. It can be attributed to the microsolubility of glucose in ethanol. When the solvent was evaporated to dryness, the dissolved and then crystallised out glucose surface could not achieve uniform contact with TBOT. When petroleum ether and methanol, which are insoluble in glucose, were chosen as reaction solvents, both gave rutile contents similar to that of C_8H_{18}, showing the universality of this strategy. Maintains Solid Polyol (e.g., glucose) in its solid state, ensuring the thorough progress of the surface/interface transesterification reaction. Retains its solid state during the reaction, a prerequisite for spatially restricting transesterification to the surface/interface and controlling the reversible reaction kinetics.

As shown in Figure 5E, by selecting different titanium sources, including TTIP, titanium oxysulfate ($TiOSO_4$), and titanium tetrachloride ($TiCl_4$), all at a G/Ti ratio of 30:1 (denoted as GT30-TTIP, GT30-$TiOSO_4$ and GT30-$TiCl_4$, respectively). Notably, the GT30-$TiCl_4$ system, employing titanium tetrachloride ($TiCl_4$) as the titanium source, also demonstrated a significant presence of the rutile phase. This phenomenon is attributed to alterations in the connection mode of the TiO_6 octahedra subsequent to dehydration crosslinking, which is induced by the coordination of chloride ions (Cl^-) to titanium ions (Ti^{4+})[34]. Furthermore, the ionic bonding formed between Ti^{4+} and oxide ions (O^{2-}) in titanium oxysulfate ($TiOSO_4$) hinders the transesterification reaction with glucose. When TTIP is used as a titanium source, its phase selectivity for TiO_2 is similar to that of TBOT, indicating that TTIP has the potential to serve as a candidate substrate for polyol-solid surface/interface transesterification strategy. Above all, Ti source participates in surface/interface transesterification reaction with surface hydroxyls on solid polyols to form GTC.

Additionally, various polyol-soild substrates were employed, such as pentaerythritol, fructose, sucrose, and D-(+)-Trehalose dihydrate, each maintaining a molar ratio of 30:1 with TBOT [denoted as GT30-Pentaerythritol, GT30-Fructose, GT30-Sucrose and GT30-D-(+)-Trehalose dihydrate, respectively]. Polarizing microscope images of solid polyol sucrose, D-fructose and D-(+)- Trehalose dihydrate microcrystals are shown in Supplementary Figures 4-6. The results of these syntheses are detailed in Figure 5E. As shown in Figure 5F, since there is still a large number of difficult-to-solidify reaction precursors in the intermediates of TBOT with glycerol and pentaerythritol, only anatase phase TiO_2 and a very small amount of rutile phase TiO_2 can be formed after annealing process. XRD analysis of the A/R TiO_2 HPJs, with the exception of those involving glycerol and pentaerythritol, displayed characteristic diffraction peaks near 25° and 27°. These peaks are indicative of the anatase and rutile phases, respectively, suggesting that all other solid polyols have the capability to form GTC through this transesterification approach. Furthermore, the absence of peaks corresponding to the polyol substrates in the diffractograms implies that the calcination process effectively eliminates all organic constituents. The conditions and results of the above experiments have been summarized in Table 1. These findings affirm that this polyol-solid surface/interface transesterification strategy offers a flexible and environmentally benign approach for the tailored synthesis of A/R TiO_2 HPJs. This strategy not only provides a convincing alternative for the synthesis strategy of A/R TiO_2 HPJs, but also paves the way for potential application prospects.

The photocatalytic performance of A/R TiO_2 HPJs GTx (x = 0, 5, 15, 20, 30 and 35) was assessed through the photocatalytic precipitation of hydrogen from artificial seawater, facilitated by illumination from a 300 W xenon lamp. Due to the limited photocatalytic activity of bulk titanium dioxide in seawater, tests were conducted by loading platinum (Pt) as a co-catalyst. The quantity of Pt loaded was quantified using inductively coupled plasma optical emission spectroscopy (ICP-OES), as detailed in Supplementary Table 2.

Figure 6A and B illustrates the photocatalytic decomposition rates of seawater for hydrogen production across various photocatalyst formulations. In the photocatalytic tests of simulation seawater splitting, Pt was selected as the co-catalyst, and its loading was determined by ICP-OES, as detailed in Supplementary Table 3. Notably, the incorporation of the rutile phase markedly enhances the photocatalytic efficiency. Among the tested compositions, GT15 demonstrated the most superior photocatalytic hydrogen production rate, achieving 5,787.7 $\mu mol \cdot h^{-1} \cdot g^{-1}$. This rate significantly surpasses those observed for GT5 (1,817.4 $\mu mol \cdot h^{-1} \cdot g^{-1}$), GT20 (2,640.4 $\mu mol \cdot h^{-1} \cdot g^{-1}$), GT30 (749.7 $\mu mol \cdot h^{-1} \cdot g^{-1}$), and the rates recorded for the monophasic TiO_2 (1,323.6 $\mu mol \cdot h^{-1} \cdot g^{-1}$ for GT0 and a markedly lower 22.8 $\mu mol \cdot h^{-1} \cdot g^{-1}$ for GT35). The enhanced performance of GT15 is attributed to the maximum coating of rutile TiO_2 by anatase TiO_2, which maximizes the number of anatase/rutile interfaces [Figure 2C1]. In addition, the effect of the crystal phase composition of A/R TiO_2 HPJs photocatalysts on the photocatalytic activity was investigated in detail. The hydrogen generation rate showed an increasing and then decreasing trend with the increase of rutile proportion [Figure 6C]. The hydrogen production rate of GT15 reached a maximum value of 5,787.7 $\mu mol \cdot h^{-1} \cdot g^{-1}$ when the rutile content was 31.54%. The presence of a small amount of rutile phase (31.54 wt%) and a large amount of anatase phase (68.46 wt%) increased the H_2 production rate of the dominant anatase phase (100 wt% anatase and 0 wt% rutile) from 1,323.6 $\mu mol \cdot h^{-1} \cdot g^{-1}$ to 5,787.7 $\mu mol \cdot h^{-1} \cdot g^{-1}$. However, when the proportion of the rutile phase was further increased to the dominant rutile (0 wt% of anatase), the H_2 yield decreased sharply to nearly 0, which originated from the poor photocatalytic activity of rutile TiO_2[73]. Due to the optimized interface engineering, when the phase interface contact between the two phases is maximized, the optimal photocatalytic performance is demonstrated. These experimental outcomes conclusively demonstrate that anatase-rutile heterophase interfaces substantially amplify the photocatalytic efficiency of A/R TiO_2 HPJs.

Table 1. Substrate scope for polyol-soild surface/interface transesterification strategy of various polyols and ti sources

Entry	Substrate	Ti (IV) source	Temperature (°C)	Time (min)	Anatase (wt%)	Rutile (wt%)
1			80	120	95.96	4.04
2			80	60	93.25	6.75
3			80	60	31.95	68.05
4			80	60	13.90	86.10
5			80	60	22.32	76.67
6			80	60	73.13	26.87
7		$TiCl_4$	80	60	76.79	23.21
8		$TiOSO_4$	80	60	100	0
9			80	60	38.01	61.99

The cycling test [Figure 6D] demonstrated that GT15 had sustained high photocatalytic activity and could last for 25 h of photocatalytic cycles without showing a significant decrease in performance. Additionally, the XRD images post-cycling [Figure 6E] indicated that the structure of the synthesized photocatalysts remained unchanged, even under the prolonged exposure to high concentrations of inorganic salts in simulated seawater. These findings underscore the excellent corrosion resistance and cyclic stability of the photocatalysts. The UV-visible diffuse reflectance spectroscopy (UV-Vis DRS) profiles of GTx (where x = 0, 5, 15, 20, 30 and 35) are presented in Figure 6F. These profiles distinctly illustrate an incremental enhancement in the absorption of the photocatalysts within the UV region (< 420 nm) of the solar spectrum, corresponding to the increasing rutile phase content. This enhancement in absorption can be ascribed to the relatively wider bandgap of the rutile phase in comparison to that of the anatase phase[74]. Meanwhile, the light absorption capacities of all samples without Pt loading were analyzed using UV-Vis DRS, as depicted in Supplementary Figure 7A-F. The absorption edges of the GT0 are situated around 428 nm. In contrast, the absorption edge of other samples shifts to a longer wavelength (GT5: 429 nm, GT15: 429 nm, GT20: 432 nm and GT30: 432 nm) indicating a slightly enhanced light absorption capability of the A/R TiO_2 HPJs. Additionally, band gap evaluations of all samples are presented in Supplementary Figure 7. From Supplementary Figure 7G, it is evident that GT0 has band gaps of 2.86 eV. Supplementary Figure 7H-K displays band gaps of GT5, GT15, GT20 and GT30 exhibiting band gaps of 2.74, 2.73, 2.72 and 2.72 eV, respectively, reinforcing that with the increase of rutile phase content, the band gap of the photocatalyst gradually narrowed[75,76]. Supplementary Figure 7L displays band gaps of pure rutile GT35 exhibiting band gaps of 2.71 eV. The observed discrepancies in band gap energies relative to literature values for pristine materials arise from particle dimension variations and UV-vis spectroscopic probe penetration depth limitations.

The photocatalytic performance of as-prepared catalysts was assessed through RhB degradation kinetics analysis. As can be seen from Figure 6G and H, GT15 showed the highest activity (order: GT15 > GT20 > GT30 > GT35 (rutile) > GT5 > GT0 (anatase)) compared to GT0, GT5, GT20, GT30 and GT35. This result was consistent with the hydrogen production performance. After 90 min irradiation, the degradation rate of RhB by GT15 reached 98.71%. The degradation kinetics of distinct samples were modeled using

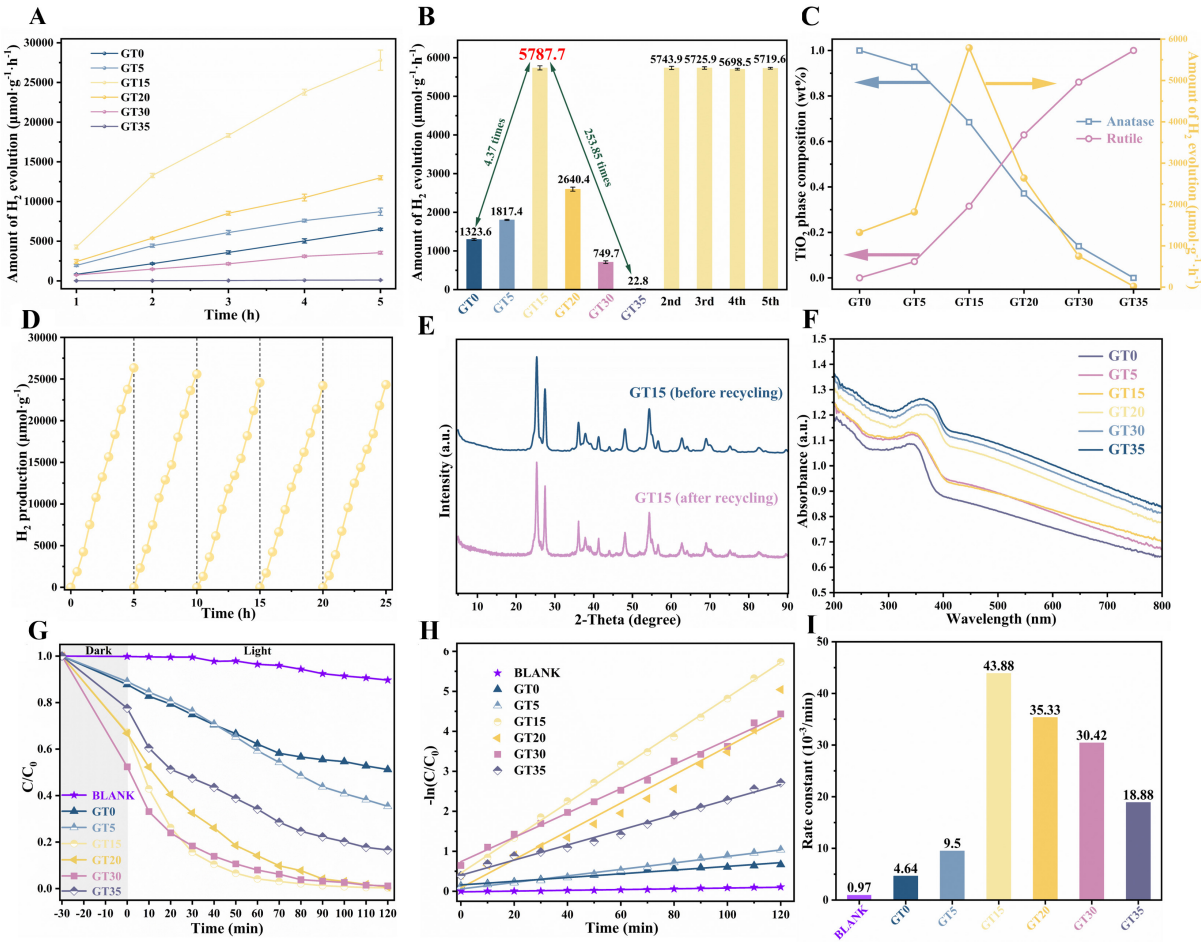

Figure 6. (A) Time course of H_2 evolution; (B) Photocatalytic performance of GTx (x = 0, 5, 15, 20, 30 and 35) for H_2 production and the stability of GT15 during H_2 production in simulated seawater. In standard photocatalytic testing, Pt was employed as the co-catalyst while methanol served as the sacrificial agent; (C) Correlations between the phase structure and specific mass photocatalytic H_2 yield of GTx HPJs; (D) Stability of GT15 during H_2 production in simulated seawater; (E) XRD patterns of GT15 sample before and after recycling test; (F) UV-Vis DRS of GT0, GT5, GT15, GT20, GT30 and GT35 after Pt loading; (G) Efficiency curves of GTx (x = 0, 5, 15, 20, 30 and 35) photocatalytic degradation to RhB; (H) Corresponding degradation kinetic; (I) Photodegradation rate constant of GTx (x=0, 5, 15, 20, 30 and 35). XRD: X-ray diffraction; UV-Vis DRS: UV-visible diffuse reflectance spectroscopy; GTx HPJs: anatase/rutile TiO_2 heterophase junctions.

pseudo-first-order reaction dynamics. The rate constant k was derived through

$$\ln(C/C_0) = kt \quad (2)$$

where k represents the rate constant (min^{-1}), t corresponds to reaction duration, C_0 signifies the initial concentration, and C indicates the residual concentration at time t. Kinetic analysis of the degradation process [Figure 6I] reveals the limited photocatalytic efficiency of anatase TiO_2 (GT0) and rutile TiO_2 (GT35). Interestingly, GT20, GT30, and GT35 exhibited excellent dark reaction efficiencies attributed to the increase in specific surface area [Supplementary Table 4], which is consistent with the mechanism shown in Figure 2A3-E3.

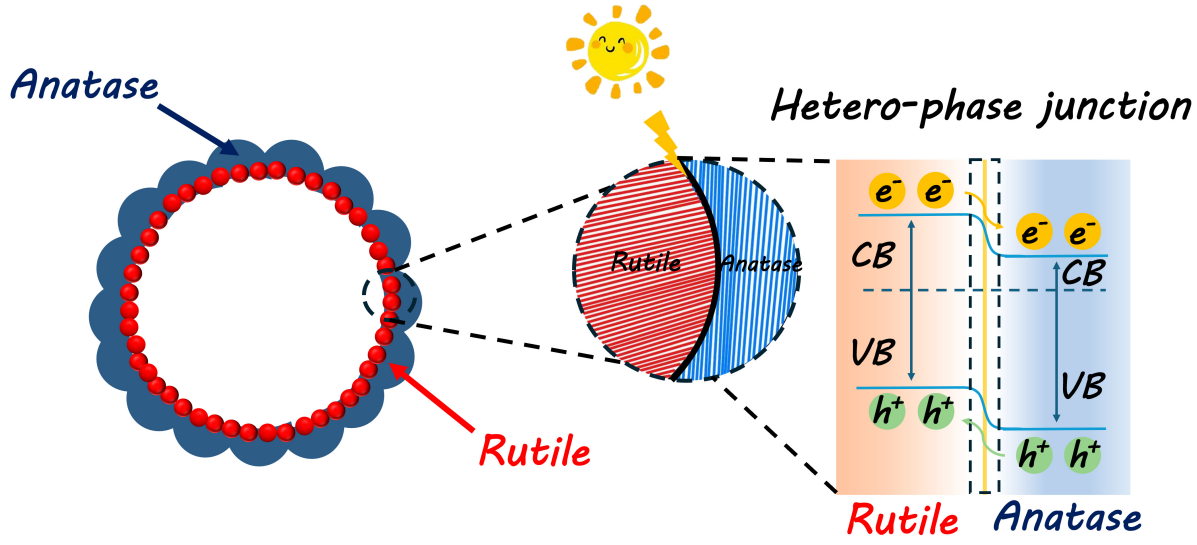

Figure 7. Diagram of photogenerated charges transfer and distribution between rutile and anatase TiO_2.

Based on the above analysis, the enhanced significantly photocatalytic performance of sample GT15 is mainly attributed to (i) the precisely controllable phase composition; The optimal rutile phase ratio (31.54%) was found to optimize interfacial synergy effects between anatase and rutile phases, enhancing charge carrier separation and transport efficiency across heterophase junctions; (ii) The matched band alignment; Atomic-level interface contact between anatase and rutile TiO_2 facilitate the transfer efficiency of e^--h^+ pairs[77,78] [Figure 7], and (iii) maximum contact of the phase interface; The heterophase architecture with abundant interfacial domains effectively prolongs the charge carrier lifetime by providing continuous transfer pathways and sufficient reactive sites, thereby synergistically enhancing the overall quantum efficiency of photocatalytic reactions.

CONCLUSIONS

In summary, this study successfully developed a facile polyol-solid surface/interface transesterification strategy for the precise synthesis of A/R TiO_2 HPJs photocatalysts with tailored phase composition. In this strategy, the transesterification product glucose titanate GTC is the key to forming the rutile phase through annealing at milder temperatures. Meanwhile, the content of GTC can be conveniently regulated by adjusting the G/Ti ratio. Thus, tunable control over phase configuration (rutile: 0%-100%) is enabled through systematic adjustment of the G/Ti ratio. Interestingly, surface area correlation of polyol-solid surface/interface transesterification strategy was proved by grinding the glucose particles, which is reflected in an increase in the slope of the Rutile content-G/Ti linear fitting results. Besides, this work explores the solvent-, solid polyol-, and Ti source-relevance of this process to expand the universality of surface/interface transesterification strategy. The strategic surface engineering of rutile TiO_2 with optimally dispersed anatase TiO_2 domains in GT15 enables superior separation efficiency of photogenerated electron-hole pairs and enhanced charge carrier transport kinetics. Proof-of-concept application of the crystal phase dependence of A/R TiO_2 HPJs photocatalytic performance indicates that GT15 shows enhanced performance in photocatalytic HER from seawater splitting. The highest H_2 production rates reached 5,787.7 $\mu mol \cdot h^{-1} \cdot g^{-1}$, which was 4.37 and 253.85 times higher than that of pure anatase and pure rutile, respectively. Without any co-catalyst, GT15 also demonstrated the best photocatalytic performance, degrading 98.17% of 20 mg/L RhB within 90 min. This study establishes a transformative paradigm for precision phase engineering via solid-state interfacial transesterification chemistry, offering a versatile platform for architecting

photocatalytic TiO_2 systems with programmable heterophase junctions.

DECLARATIONS

Authors' contributions

Conceptualization, writing - original draft, writing - review and editing, software, resources, project administration, methodology, formal analysis, data curation: Zhang, C.
Methodology, data curation, formal analysis: Zhou, Y.; Yang, X.; Liu, K.; Ayyub, A.
Conceptualization, methodology, data curation: Li, Y.
Writing - review and editing: Lim, K. H.
Validation, writing - review and editing: Zheng, W.; Xu, M.
Writing - review and editing, visualization, resources, funding acquisition, formal analysis, data curation, conceptualization: Yang, W.
Resources, writing - review and editing: Kawi, S.

Availability of data and materials

The original contributions presented in this study are included in the article/Supplementary Materials. Further inquiries can be directed to the corresponding author(s).

Financial support and sponsorship

This work was financially supported by the National Natural Science Foundation of China (Grant No. 22162008), the Science and Technology Supporting Project of Guizhou Province [Grant No. (2022)208], and the Guizhou Province Local Government Overseas Study Program.

Conflicts of interest

All authors declared that there are no conflicts of interest.

Ethical approval and consent to participate

Not applicable.

Consent for publication

Not applicable.

Copyright

© The Author(s) 2025.

REFERENCES

1. Motesharrei, S.; Rivas, J.; Kalnay, E.; et al. Modeling sustainability: population, inequality, consumption, and bidirectional coupling of the earth and human systems. *Natl. Sci. Rev.* **2016**, *3*, 470-94. DOI PubMed PMC
2. Feng, L.; Yu, H.; Yang, G.; et al. Novel 3D@2D/2D HHSS@BiOBr/$Znln_2S_4$ S-scheme photocatalyst for efficient adsorption-photocatalytic-photosensitization synergistic degradation of organics. *Appl. Surf. Sci.* **2023**, *640*, 158340. DOI
3. Bolson, N.; Prieto, P. T. Capacity factors for electrical power generation from renewable and nonrenewable sources. *Proc. Natl. Acad. Sci. U. S. A.* **2022**, *119*, 52. DOI PubMed PMC
4. Wang, M.; Liu, S.; Qian, T.; et al. Over 56.55% faradaic efficiency of ambient ammonia synthesis enabled by positively shifting the reaction potential. *Nat. Commun.* **2019**, *10*, 341. DOI PubMed PMC
5. Wang, H.; Zou, Y.; Sun, H.; Chen, Y.; Li, S.; Lan, Y. Recent progress and perspectives in heterogeneous photocatalytic CO_2 reduction through a solid-gas mode. *Coord. Chem. Rev.* **2021**, *438*, 213906. DOI
6. Liu, M.; Wei, C.; Zhuzhang, H.; et al. Fully condensed poly (triazine imide) crystals: extended π-conjugation and structural defects for overall water splitting. *Angew. Chem. Int. Ed.* **2022**, *61*, e202113389. DOI
7. Yan, Y.; Lin, J.; Huang, K.; et al. Tensile strain-mediated spinel ferrites enable superior oxygen evolution activity. *J. Am. Chem. Soc.* **2023**, *145*, 24218-29. DOI
8. Zhou, W.; Li, F.; Yang, X.; et al. Peanut-chocolate-ball-inspired construction of the interface engineering between CdS and intergrown

Cd: boosting both the photocatalytic activity and photocorrosion resistance. *J. Energy. Chem.* **2023**, *76*, 75-89. DOI
9. Chen, X.; Zhao, J.; Li, G.; Zhang, D.; Li, H. Recent advances in photocatalytic renewable energy production. *Energy. Mater.* **2022**, *2*, 200001. DOI
10. Phongamwong, T.; Barrabés, N.; Donphai, W.; Witoon, T.; Rupprechter, G.; Chareonpanich, M. Chlorophyll-modified $Au_{25}(SR)_{18}$-functionalized TiO_2 for photocatalytic degradation of rhodamine B. *Appl. Catal. B. Environ.* **2023**, *325*, 122336. DOI
11. Ruan, X.; Zhao, S.; Xu, M.; et al. Iso-elemental $ZnIn_2S_4$/$Zn_3In_2S_6$ heterojunction with low contact energy barrier boosts artificial photosynthesis of hydrogen peroxide. *Adv. Energy. Mater.* **2024**, *14*, 2401744. DOI
12. Ruan, X.; Cui, X.; Cui, Y.; et al. Favorable energy band alignment of TiO_2 anatase/rutile heterophase homojunctions yields photocatalytic hydrogen evolution with quantum efficiency exceeding 45.6%. *Adv. Energy. Mater.* **2022**, *12*, 2200298. DOI
13. Li, S.; He, H.; Li, X.; et al. Construction of Cu-doped α-Fe_2O_3/γ-Fe_2O_3 hetero-phase junction composite and its photocatalytic performance. *Chem. Eng. J.* **2024**, *501*, 157678. DOI
14. Fujishima, A. H. K. Electrochemical photolysis of water at a semiconductor electrode. *Nature* **1972**, *238*, 37-38. DOI
15. Linsebigler, A. L.; Lu, G.; Yates, J. T. Photocatalysis on TiO_2 surfaces: principles, mechanisms, and selected results. *Chem. Rev.* **1995**, *95*, 735-58. DOI
16. Liu, M.; Qiu, X.; Miyauchi, M.; Hashimoto, K. Cu(II) oxide amorphous nanoclusters grafted Ti^{3+} Self-Doped TiO_2: an efficient visible light photocatalyst. *Chem. Mater.* **2011**, *23*, 5282-6. DOI
17. Chen, X.; Selloni, A. Introduction: titanium dioxide (TiO_2) nanomaterials. *Chem. Rev.* **2014**, *114*, 9281-2. DOI PubMed
18. Mishra, P. R.; Srivastava, O. N. On the synthesis, characterization and photocatalytic applications of nanostructured TiO_2. *Bull. Mater. Sci.* **2008**, *31*, 545-50. DOI
19. Puddu, V.; Choi, H.; Dionysiou, D. D.; Puma, G. L. TiO_2 photocatalyst for indoor air remediation: Influence of crystallinity, crystal phase, and UV radiation intensity on trichloroethylene degradation. *Appl. Catal. B. Environ.* **2010**, *94*, 211-8. DOI
20. Roy, P.; Berger, S.; Schmuki, P. TiO_2 nanotubes: synthesis and applications. *Angew. Chem. Int. Ed.* **2011**, *50*, 2904-39. DOI
21. Kyriaki, E. Karakitsou XEV. Effects of altervalent cation doping of titania on its performance as a photocatalyst for water cleavage. *J. Phys. Chem. C.* **1993**, *97*, 1184-9. DOI
22. Feng, Y.; Zhang, Y.; Wang, J.; et al. Promotion of anatase/rutile junction to direct conversion of syngas to ethanol on the Rh/TiO_2 catalysts. *ACS. Catal.* **2024**, *14*, 1874-81. DOI
23. Cho, I. S.; Chen, Z.; Forman, A. J.; et al. Branched TiO_2 nanorods for photoelectrochemical hydrogen production. *Nano. Lett.* **2011**, *11*, 4978-84. DOI
24. Wang, H.; Chen, J.; Xiao, F.; Zheng, J.; Liu, B. Doping-induced structural evolution from rutile to anatase: formation of Nb-doped anatase TiO_2 nanosheets with high photocatalytic activity. *J. Mater. Chem. A.* **2016**, *4*, 6926-32. DOI
25. Li, B.; Zheng, H.; Zhou, T.; et al. Revealing the synergistic effect of bulk and surface co-doped boron on TiO_2 for enhanced photocatalytic H_2 evolution. *Chem. Eng. J.* **2024**, *497*, 154726. DOI
26. Wang, G.; Wang, H.; Ling, Y.; et al. Hydrogen-treated TiO_2 nanowire arrays for photoelectrochemical water splitting. *Nano. Lett.* **2011**, *11*, 3026-33. DOI
27. Choi, S. Y.; Kim, S.; Lee, K. J.; Kim, J. Y.; Han, D. S.; Park, H. Solar hydrogen peroxide production on carbon nanotubes wired to titania nanorod arrays catalyzing As(III) oxidation. *Appl. Catal. B. Environ.* **2019**, *252*, 55-61. DOI
28. Xiao, L.; Spies, J. A.; Sheehan, C. J.; et al. Electron transfer dynamics at dye-sensitized SnO_2/TiO_2 core/shell electrodes in aqueous/nonaqueous electrolyte mixtures. *J. Am. Chem. Soc.* **2024**, *146*, 18117-27. DOI
29. Liu ESA. Growth of oriented single-crystalline rutile TiO_2 nanorods on transparent conducting substrates for dye-sensitized solar cells. *J. Am. Chem. Soc.* **2009**, *131*, 3985-90. DOI
30. Zhang, P.; Tian, Z.; Kang, Y.; et al. Sub-10 nm corrugated TiO_2 nanowire arrays by monomicelle-directed assembly for efficient hole extraction. *J. Am. Chem. Soc.* **2022**, *144*, 20964-74. DOI
31. Wu, J.; Zhang, Y.; Lu, P.; et al. Engineering 2D multi-hetero-interface in the well-designed nanosheet composite photocatalyst with broad electron-transfer channels for highly-efficient solar-to-fuels conversion. *Appl. Catal. B. Environ.* **2021**, *286*, 119944. DOI
32. Zhang, D.; Liu, W.; Wang, R.; Zhang, Z.; Qiu, S. Interface engineering of hierarchical photocatalyst for enhancing photoinduced charge transfers. *Appl. Catal. B. Environ.* **2021**, *283*, 119632. DOI
33. Zhou, Y.; Yang, W.; Feng, L.; Hong, J.; Abbas, M.; Kawi, S. Sunflower-disc-inspired vertical growth of 2D $ZnIn_2S_4$ on ultra-thin TiO_2 : Constructing a 3D porous photocatalytic glass film for ultra-efficient organic pollutant degradation. *Appl. Catal. B. Environ. Energy.* **2025**, *363*, 124782. DOI
34. Peng, C.; Zhou, T.; Wei, P.; et al. Regulation of the rutile/anatase TiO_2 phase junction in-situ grown on -OH terminated $Ti_3C_2T_x$ (MXene) towards remarkably enhanced photocatalytic hydrogen evolution. *Chem. Eng. J.* **2022**, *439*, 135685. DOI
35. Cho, M.; Younis, S. A.; Lee, C. S.; Li, X.; Kim, K. The superior mineralization potential of a graphitic carbon nitride/titanium dioxide composite and its application in the construction of a portable photocatalytic air purification system against gaseous formaldehyde. *J. Mater. Chem. A.* **2024**, *12*, 32239-58. DOI
36. Navakoteswara, R. V.; Kwon, H.; Lee, Y.; et al. Synergistic integration of MXene nanosheets with CdS@TiO_2 core@shell S-scheme photocatalyst for augmented hydrogen generation. *Chem. Eng. J.* **2023**, *471*, 144490. DOI
37. Yang, G.; Ding, H.; Chen, D.; Feng, J.; Hao, Q.; Zhu, Y. Construction of urchin-like $ZnIn_2S_4$-Au-TiO_2 heterostructure with enhanced activity for photocatalytic hydrogen evolution. *Appl. Catal. B. Environ.* **2018**, *234*, 260-7. DOI
38. Cui, P.; Qu, S.; Zhang, Q.; et al. Homojunction perovskite solar cells: opportunities and challenges. *Energy. Mater.* **2022**, *1*, 100014.

DOI

39. Zhang, Y.; Cao, Q.; Meng, A.; et al. Molecular heptazine-triazine junction over carbon nitride frameworks for artificial photosynthesis of hydrogen peroxide. *Adv. Mater.* **2023**, *35*, 2306831. DOI
40. Liu, J.; Yu, X.; Liu, Q.; et al. Surface-phase junctions of branched TiO_2 nanorod arrays for efficient photoelectrochemical water splitting. *Appl. Catal. B. Environ.* **2014**, *158-9*, 296-300. DOI
41. Chen, K.; Li, G.; Hu, Z.; et al. Construction of γ-MnS/α-MnS hetero-phase junction for high-performance sodium-ion batteries. *Chem. Eng. J.* **2022**, *435*, 135149. DOI
42. Ren, H.; Yu, R.; Qi, J.; Zhang, L.; Jin, Q.; Wang, D. Hollow multishelled heterostructured anatase/TiO_2(B) with superior rate capability and cycling performance. *Adv. Mater.* **2019**, *31*, 1805754. DOI
43. Liu, C.; Zheng, L.; Song, Q.; et al. A Metastable crystalline phase in two-dimensional metallic oxide nanoplates. *Angew. Chem. Int. Ed.* **2019**, *58*, 2055-9. DOI
44. Zhang, J.; Xu, Q.; Feng, Z.; Li, M.; Li, C. Importance of the relationship between surface phases and photocatalytic activity of TiO_2. *Angew. Chem. Int. Ed.* **2008**, *47*, 1766-9. DOI
45. Jiang, Y.; Zhao, W.; Li, S.; et al. Elevating photooxidation of methane to formaldehyde via TiO_2 crystal phase engineering. *J. Am. Chem. Soc.* **2022**, *144*, 15977-87. DOI
46. Chen, X.; Liu, L.; Yu, P. Y.; Mao, S. S. Increasing solar absorption for photocatalysis with black hydrogenated titanium dioxide nanocrystals. *Science* **2011**, *331*, 746-50. DOI
47. Yan, P.; Wang, X.; Zheng, X.; et al. Photovoltaic device based on TiO_2 rutile/anatase phase junctions fabricated in coaxial nanorod arrays. *Nano. Energy.* **2015**, *15*, 406-12. DOI
48. Zhang, W.; He, H.; Tian, Y.; et al. Synthesis of uniform ordered mesoporous TiO_2 microspheres with controllable phase junctions for efficient solar water splitting. *Chem. Sci.* **2019**, *10*, 1664-70. DOI
49. Tomita, K.; Petrykin, V.; Kobayashi, M.; Shiro, M.; Yoshimura, M.; Kakihana, M. A water-soluble titanium complex for the selective synthesis of nanocrystalline brookite, rutile, and anatase by a hydrothermal method. *Angew. Chem. Int. Ed.* **2006**, *45*, 2378-81. DOI PubMed
50. Lei, W.; Wang, Y.; Wang, H.; Suzuki, N.; Terashima, C.; Fujishima, A. Gelation-induced controlled synthesis of TiO_2 with tunable phase transition for efficient photocatalytic hydrogen evolution. *Inorg. Chem. Front.* **2024**, *11*, 2178-86. DOI
51. Rao, K. V. K.; Naidu, S. V. N.; Iyengar, L. Thermal expansion of rutile and anatase. *J. Am. Ceram. Soc.* **1970**, *53*, 124-6. DOI
52. Koirala, R.; Pratsinis, S. E.; Baiker, A. Synthesis of catalytic materials in flames: opportunities and challenges. *Chem. Soc. Rev.* **2016**, *45*, 3053-68. DOI PubMed
53. Zhang, X.; Chen, J.; Jiang, S.; et al. Enhanced photocatalytic degradation of gaseous toluene and liquidus tetracycline by anatase/rutile titanium dioxide with heterophase junction derived from materials of Institut Lavoisier-125(Ti): degradation pathway and mechanism studies. *J. Colloid. Interface. Sci.* **2021**, *588*, 122-37. DOI
54. Peng, C.; Wang, H.; Yu, H.; Peng, F. (111) TiO_{2-x}/Ti_3C_2: synergy of active facets, interfacial charge transfer and Ti^{3+} doping for enhance photocatalytic activity. *Mater. Res. Bull.* **2017**, *89*, 16-25. DOI
55. Xia, X.; Peng, S.; Bao, Y.; et al. Control of interface between anatase TiO_2 nanoparticles and rutile TiO_2 nanorods for efficient photocatalytic H_2 generation. *J. Power. Sources.* **2018**, *376*, 11-7. DOI
56. Choi, H. C.; Jung, Y. M.; Kim, S. B. Size effects in the Raman spectra of TiO_2 nanoparticles. *Vib. Spectrosc.* **2005**, *37*, 33-8. DOI
57. Brouwer, D. H.; Mikolajewski, J. G. A combined solid-state NMR and quantum chemical calculation study of hydrogen bonding in two forms of α-d-glucose. *Solid. State. Nucl. Magn. Reson.* **2023**, *123*, 101848. DOI PubMed
58. Carnahan, S. L.; Chen, Y.; Wishart, J. F.; Lubach, J. W.; Rossini, A. J. Magic angle spinning dynamic nuclear polarization solid-state NMR spectroscopy of γ-irradiated molecular organic solids. *Solid. State. Nucl. Magn. Reson.* **2022**, *119*, 101785. DOI PubMed
59. Pisklak, D. M.; Zielińska-Pisklak, M. A.; Szeleszczuk, Ł.; Wawer, I. ^{13}C solid-state NMR analysis of the most common pharmaceutical excipients used in solid drug formulations, Part I: chemical shifts assignment. *J. Pharm. Biomed. Anal.* **2016**, *122*, 81-9. DOI PubMed
60. Wang, J.; Yu, T.; Wang, M.; Guo, X.; Chen, Y. A novel biochar-composed TiO_2 (BC-Ti) for efficient photocatalytic degradation on arbidol. *J. Ind. Eng. Chem.* **2024**, *134*, 537-47. DOI
61. Bibi, S.; Ahmad, A.; Anjum, M. A. R.; et al. Photocatalytic degradation of malachite green and methylene blue over reduced graphene oxide (rGO) based metal oxides (rGO-Fe_3O_4/TiO_2) nanocomposite under UV-visible light irradiation. *J. Environ. Chem. Eng.* **2021**, *9*, 105580. DOI
62. Shah, A. H.; Rather, M. A. Effect of calcination temperature on the crystallite size, particle size and zeta potential of TiO_2 nanoparticles synthesized via polyol-mediated method. *Mater. Today. Proc.* **2021**, *44*, 482-8. DOI
63. Peng, C.; Wei, P.; Chen, X.; et al. A hydrothermal etching route to synthesis of 2D MXene (Ti_3C_2, Nb_2C): enhanced exfoliation and improved adsorption performance. *Ceram. Int.* **2018**, *44*, 18886-93. DOI
64. Zhou, T.; Wu, C.; Wang, Y.; et al. Super-tough MXene-functionalized graphene sheets. *Nat. Commun.* **2020**, *11*, 2077. DOI PubMed PMC
65. Midya, P.; Sarngan, P. P.; Dutta, A.; Kumar, C. K.; Sarkar, D. Carbon-modified TiO_2 nanourchin with Ag nanoparticle decoration for environmental remediation. *Mater. Sci. Eng. B.* **2022**, *286*, 116028. DOI
66. Gao, P.; Shi, H.; Ma, T.; et al. MXene/TiO_2 heterostructure-decorated hard carbon with stable Ti-O-C bonding for enhanced sodium-ion storage. *ACS. Appl. Mater. Interfaces.* **2021**, *13*, 51028-38. DOI

67. Roldán, M. V.; Porta, E.; Durán, A.; Castro, Y.; Pellegri, N. Development of photocatalysts based on TiO_2 films with embedded Ag nanoparticles. *Int. J. Appl. Glass. Sci.* **2022**, *13*, 429-43. DOI
68. With, P. C.; Helmstedt, U.; Naumov, S.; et al. Low-temperature photochemical conversion of organometallic precursor layers to titanium(IV) oxide thin films. *Chem. Mater.* **2016**, *28*, 7715-24. DOI
69. Chen, J.; Mu, L.; Jiang, B.; Yin, H.; Song, X.; Li, A. TG/DSC-FTIR and Py-GC investigation on pyrolysis characteristics of petrochemical wastewater sludge. *Bioresour. Technol.* **2015**, *192*, 1-10. DOI
70. Lovatti, B. P.; Silva, S. R.; Portela, N. D. A.; et al. Identification of petroleum profiles by infrared spectroscopy and chemometrics. *Fuel* **2019**, *254*, 115670. DOI
71. Özsin, G.; Pütün, A. E. Kinetics and evolved gas analysis for pyrolysis of food processing wastes using TGA/MS/FT-IR. *Waste. Manag.* **2017**, *64*, 315-26. DOI PubMed
72. Fan, Q. G.; Lewis, D. M.; Tapley, K. N. Characterization of cellulose aldehyde using Fourier transform infrared spectroscopy. *J. Appl. Polym. Sci.* **2001**, *82*, 1195-202. DOI
73. Tracy, L. Thompson and John T. Yates J. Surface science studies of the photoactivation of TiO_2-new photochemical processes. *Chem. Rev.* **2006**, *106*, 4428-53. DOI
74. Ding, Y.; Yang, I. S.; Li, Z.; et al. Nanoporous TiO_2 spheres with tailored textural properties: controllable synthesis, formation mechanism, and photochemical applications. *Prog. Mater. Sci.* **2020**, *109*, 100620. DOI
75. Scanlon, D. O.; Dunnill, C. W.; Buckeridge, J.; et al. Band alignment of rutile and anatase TiO_2. *Nat. Mater.* **2013**, *12*, 798-801. DOI
76. Apopei, P.; Catrinescu, C.; Teodosiu, C.; Royer, S. Mixed-phase TiO_2 photocatalysts: crystalline phase isolation and reconstruction, characterization and photocatalytic activity in the oxidation of 4-chlorophenol from aqueous effluents. *Appl. Catal. B. Environ.* **2014**, *160-161*, 374-82. DOI
77. Gao, Y.; Zhu, J.; An, H.; et al. Directly probing charge separation at interface of TiO_2 phase junction. *J. Phys. Chem. Lett.* **2017**, *8*, 1419-23. DOI
78. Qu, J.; He, J.; Li, H.; et al. Unraveling the role of interface in photogenerated charge separation at the anatase/rutile heterophase junction. *J. Phys. Chem. C.* **2023**, *127*, 768-75. DOI